


Article

UV Solar Energy and Erythemat Exposure: Mathematical Models to Assess the Dose on Vertical and Inclined Planes in Different Sky Conditions

Chiara Burattini ^{1,*} , Massimo Borra ², Flavia Vespasiano ¹ and Fabio Bisegna ¹

¹ Department of Astronautical Electrical and Energy Engineering, Sapienza University, 00184 Rome, Italy; flavia.vespasiano@uniroma1.it (F.V.); fabio.bisegna@uniroma1.it (F.B.)

² Department of Occupational and Environmental Medicine, Epidemiology and Hygiene, Italian Workers Compensation Authority (INAIL), 00078 Monte Porzio Catone, Italy; m.borra@inail.it

* Correspondence: chiara.burattini@uniroma1.it; Tel.: +39-0644585432

Abstract: Ultra violet (UV) solar energy can cause several negative effects to the skin and eyes in case of overexposure. To protect people from erythemat damage, personal erythemat exposure must be carefully assessed when outdoor activities are carried out. The direct measure with scientific instruments is impracticable to common people, and indirect methods assess the exposure only on the horizontal plane: this work developed a mathematical model to assess erythemat exposure to all the body districts. UVA irradiance and erythemat irradiance were measured on several inclined planes, oriented to the four cardinal directions, in seven environments with multiple sky conditions. The UV erythemat (UVE) ratio between erythemat irradiance on an inclined plane (I_{ery}°) and UVA irradiance on a horizontal plane (IUVAh) was calculated. The results indicate that the $UVE = I_{ery}^\circ / IUVAh$ is variable across the day and depends on the plane orientation, its degree of inclination, and sky conditions. Mathematical models to calculate erythemat exposure in clear, intermediate and overcast sky conditions on planes with different inclinations and orientations were derived from the daily trends of the $UVE = I_{ery}^\circ / IUVAh$. The application procedure of the mathematical model to the vertical plane oriented to the south is provided as an example.

Keywords: UV solar radiation; erythemat exposure; outdoor environments; orientation; inclination; human health



Citation: Burattini, C.; Borra, M.; Vespasiano, F.; Bisegna, F. UV Solar Energy and Erythemat Exposure: Mathematical Models to Assess the Dose on Vertical and Inclined Planes in Different Sky Conditions. *Energies* **2024**, *17*, 5718. <https://doi.org/10.3390/en17225718>

Academic Editor: Jesús Polo

Received: 11 September 2024

Revised: 8 November 2024

Accepted: 12 November 2024

Published: 15 November 2024



Copyright: © 2024 by the authors. Licensee MDPI, Basel, Switzerland. This article is an open access article distributed under the terms and conditions of the Creative Commons Attribution (CC BY) license (<https://creativecommons.org/licenses/by/4.0/>).

1. Introduction

Solar energy under certain conditions can be dangerous for human beings since the UV component has the capability to damage biological tissues [1]. UV is the most energetic band of the whole electromagnetic spectrum, and when an excessive amount of UV energy is received by the exposed human tissues, it can produce damage of different entities. Overexposure to solar UV energy can cause diseases to the skin [2] and eyes [3], which could be acute or chronic [4]. All this damage could affect all people carrying out outdoor activities, both for work and leisure. The World Health Organization (WHO) estimated that in 2020, about 1.2 million new cases of non-melanoma skin cancers, 325,000 cases of melanomas of the skin and 15,000 cases of people blinded by cataracts were caused by overexposure to UV radiation [5].

The erythemat effect connected to a specific condition of solar irradiation is accounted for with specific quantities. The erythemat effective irradiance [W/m^2] (erythemat irradiance in the following) derives from the UV spectral irradiance (W/m^2) with the application of the erythemat action spectrum S_λ [6,7]. The erythemat effective exposure [J/m^2] (erythemat exposure in the following), which is the erythemat irradiance level for the exposure interval of time, measures the dose received by the skin and expresses the risk of erythemat damage. Starting from the erythemat irradiance, the UV Index (UVI) was conceived to

indicate in a simple form the risk of tissue damage due to exposure to solar radiation [8]: it is a dimensionless value ranging between 1 (low risk) and 11+ (extreme risk).

The Standard Erythemal Dose (SED) was defined to quantify the erythemal effect of UV radiation on the skin: it corresponds to an erythemal exposure of 100 J/m^2 weighted with the International Commission of Illumination (CIE) erythemal action spectrum. A limit of erythemal exposure that establishes a threshold of safe exposure to solar radiation has not been defined, but in the literature, the limit of 1.0–1.3 SED is applied as indicated by the International Commission on Non-Ionizing Radiation Protection (ICNIRP) [9]. Previous works that measured the erythemal exposure of people performing different outdoor activities demonstrated that the ICNIRP limit is rapidly exceeded in summer and that at certain latitudes, it can also be exceeded in winter [10–17].

Erythemal exposure depends on the solar UV irradiance (W/m^2) received by the skin, which is influenced by atmospheric elements, weather conditions and astronomical parameters. The ozone absorption of UVB radiation reverberates on erythemal exposure [18]: time-series studies evidenced that the reduction in ozone in the atmosphere in the last decades produced an increase in daily erythemal doses [19,20]. The attenuation of UVA solar irradiance measured due to aerosol [21,22] caused a reduction in UVI [23] and in erythemal irradiance [24]. Clouds can reduce or slightly increase UV irradiance due to multiple reflections [25,26]; the attenuation or the enhancement of UV erythemal radiation depends on cloud optical thickness (COT) [27] and on the solar zenith angle (SZA) [28]. The surface albedo increases the amount of UV erythemal radiation in a percentage dependent on the surface inclination and on the SZA [29].

The level of erythemal irradiance is related to the sun's position in the sky: it assumes the maximal value at noon and minimal values at sunrise and sunset [18,30]; moreover, the highest values of erythemal irradiance can be found in summer and the lowest in winter [18,19,31].

The assessment of the erythemal exposure of a person performing an activity under the sun with a good precision level requires the use of scientific instruments [32]; measuring the erythemal exposure of every single body district irradiated by the sun is very complicated. For a correct evaluation of personal erythemal exposure, UV spectral irradiance has to be measured using a spectroradiometer for the whole exposure interval; then, the measured data have to be processed to calculate erythemal exposure. The previous procedure has to be applied to all the body districts exposed to the sun. Due to the difficulty of placing one or more spectroradiometers on the human body, usually, personal erythemal exposure is measured using dosimeters, which are wearable scientific instruments equipped with spectral filters reproducing the erythemal action spectrum [33,34]. They measure erythemal irradiance with a settable time step, and erythemal exposure has to be successively calculated. Neither of the two methods described above can be adopted by non-technical people performing outdoor activities who wish to define their actual erythemal exposure level to not exceed the safe exposure threshold of 1.0–1.3 SED.

Several applications for smartphones indicating the UVI were developed for the general public and are also available to download for free, but generally they are based on forecasting methods and do not have a good precision level [35–37]. Recently, a smart wearable device was developed that estimates personal erythemal exposure with good reliability using complex algorithms [38–40]. The device requires that the person wears the device, and this could be uncomfortable or troublesome for the activity [41]. Micro-wearable sensors detecting the amount of UV radiation received that change their color when a defined level is reached were also developed: they do not indicate the actual level of erythemal exposure, but only the cumulative UV dose [42].

Indirect methods that calculate personal erythemal exposure of body districts from the measurement of UV solar irradiance on the Earth's surface could be useful. In fact, these data are easily measurable with good precision using micro smart sensors available on the market, in addition to radiometers, and they are also provided by satellites [43,44].

Different models were developed previously in the literature that defined erythemal irradiance at the ground level integrating satellite data with meteorological variables [24,45–48]. For instance, the UVIOS system estimates the near-real-time UVI over Europe with a spatial resolution of 5 km [49], while the TROPOMI provides the erythemal dose rate, the daily erythemal dose and the UVI with good precision levels [50]. Several radiative transfer models (RTMs) [51–53] were proposed that integrated some environmental parameters to predict UV radiation; UVBoost is an estimator that applies the supervised machine learning technique to an RTM integrating UV radiation, SZA, total ozone content and aerosol optical depth and simulated the UV dose with a precision of $\pm 3\%$ [54]. Moreover, a tool to estimate the erythema dose together with DNA damage and vitamin D doses across the UK and Ireland was proposed [55].

Several studies used UV data from in situ monitoring stations to derive erythemal models. For instance, Malinovic-Milicevic et al. (2015) derived an empirical equation to assess the daily erythemal UV doses in all sky conditions correcting the clear sky measured data with total ozone and sunshine duration [56]. Recently, Garcia-Rodriguez et al. (2023) [57] developed artificial neural network models of the global horizontal erythemal irradiance for five CIE standard sky conditions using recorded climatic parameters. Gonzales-Rodriguez et al. (2021) [58] correlated hourly and daily values of horizontal erythemal irradiance with global irradiance to define empirical models of the four seasons and five sky conditions. All the previous models provide values of the erythemal quantities on the horizontal plane, which does not correctly express the exposure of the whole human body, formed by curved surfaces differently inclined and oriented: the irradiation of a surface is maximal for orthogonal incidence and decreases with angular directions until it becomes minimal for oblique rays. A general model to calculate the irradiation on inclined planes from the value measured on the horizontal one was described in Boers et al. (1998) [59]. Several studies demonstrated that vertical and inclined planes have a different exposure trend with respect to horizontal planes, and, even in general, the horizontal plane is the most exposed; in particular conditions, the irradiance on vertical surfaces can be higher than on horizontal surfaces [60–63]. For these reasons, the models that derived erythemal exposure of the human body from horizontal erythemal irradiance are very imprecise for body districts that cannot be approximated to the horizontal plane.

Soueid et al. (2022) defined a regression model of personal exposure from measurements of personal exposure and self-reported data of time spent outdoors, and it had a poor correlation with ambient UVR [64].

Some studies proposed models to predict erythemal exposure of body districts. Vernez et al. [65] defined a regression model that estimated the UV exposure ratio between the dose on the anatomic site and the dose on the ground using as input parameters the maximal SZA and the visible sky fraction of the anatomic site; the errors in calculating the daily dose from simulated data ranged from +20% to -10% . More recently, a model to estimate body exposure during beach vacations was developed: it combined a radiative transfer model with a 3D model of the human body and information related to human behavior during beach vacations to calculate the UVI and the SED on 12 body districts considering the respective clothing coverage [66]. Another study proposed a method to predict the whole exposure of the human body for adults and children, integrating the exposure ratio of the six surfaces of a cube and considering the percentage of anatomical parts not covered by clothing [67].

The aim of this work is to define mathematical models to calculate erythemal exposure (Eery) on several inclined planes, starting from horizontal values of UVA irradiance. The calculated values of erythemal exposure can refer to the exposed body districts using a simplified model of the human body [41].

2. Materials and Methods

An extensive outdoor measurement campaign was carried out in the period of spring–summer 2023 to measure UVA solar irradiance and erythral irradiance in several environmental settings under different weather conditions and on multiple planes and orientations.

The results of measurements were analyzed for separate days with the intent of defining a relation between the erythral exposure of the different planes and the horizontal UVA irradiation. Firstly, a UVE ratio was calculated for each minute of measurement; then, UVEC curves representing the trend of the UVE ratios as a function of the sun position were analyzed for each plane of measurement; successively, the UVEC curves were analyzed together for single orientations and inclinations, to define UVE mathematical models for different planes.

2.1. Measurements

The measurements of UVA solar irradiance and erythral irradiance were executed on 16 days from April to August at different hours ranging from 11:00 to 17:00 and with different conditions of sky coverage: clear sky, intermediate sky, and overcast sky. In this work, the days on which the cloud coverage was less than 10% and the sun was never obstructed were considered clear sky conditions, while the days on which the cloud coverage was more than 80% were considered overcast sky conditions; cloud coverage between 10% and 80% was considered intermediate sky conditions. To consider the difference due to the setting, the measurements took place in 7 different environments located in 4 Italian cities and towns: Rome (Lat. 41.9, Long. 12.5 and Alt. 21 m), Pineto (Lat. 42.6, Long. 14.0 and Alt. 0 m), Introacqua (Lat. 42.0, Long. 12.9 and Alt. 624 m) and Campo Imperatore (Lat. 42.4, Long. 13.5 and Alt. 2129 m). In Rome, the measurements were executed in the upper terrace of the claustrum of the Faculty of Engineering of Sapienza University (Rome-A), in the staircase at the entrance of the Faculty (Rome-B), in the square on the side of the Faculty (Rome-C) and inside the park of Ancient Appia (Rome-D); in Pineto, the setting was the beach; in Introacqua, the setting was the city garden; and in Campo Imperatore, the setting was the peak of the mountain. Table 1 describes the measurement conditions of the 16 days of data acquisition.

Table 1. Description of the measurement conditions.

Day	Place	Hour	Sky	Planes
28 April	Rome-A	11:35–13:40	clear	0° 90° E 90° W 90° N
8 May	Rome-A	11:00–12:00	overcast	0° 90° S 90° E 45° S
		12:00–13:00	overcast	0° 90° W 90° S 45° W
12 May	Rome-C	11:00–12:00	overcast	0° 90° W 90° S 60° W 45° E
		12:00–13:00	intermediate	0° 90° S 90° E 60° S 45° N
		13:00–14:00	intermediate	0° 90° E 90° N 60° E 45° W
22 May	Rome-C	11:00–12:00	clear	0° 90° S 90° N 60° N 60° S
5 June	Rome-D	13:00–14:00	overcast	0° 90° S 90° E 90° W 90° N 60° N 45° S
		14:00–15:00	overcast	0° 90° S 90° E 90° W 90° N 60° E 45° W
7 June	Rome-D	11:30–12:30	intermediate	0° 90° S 90° W 90° N 60° S 60° N 45° N
19 June	Rome-D	11:20–12:20	intermediate	0° 90° S 90° E 60° S 60° N
21 June	Campo Imperatore	12:00–16:30	clear	0° 90° S 90° E 90° N 90° W 60° S
23 June	Rome-D	11:20–12:20	clear	0° 90° S 90° E 45° N 60° N
30 June	Introacqua	12:10–13:10	intermediate	0° 90° S 60° S 45° N
1 July	Introacqua	12:30–13:30	overcast	0° 90° S 90° N 60° S 60° N 45° N
21 July	Rome-B	12:30–13:50	clear	0° 90° E 60° N 60° S 45° N

Table 1. Cont.

Day	Place	Hour	Sky	Planes
25 July	Rome-B	11:30–12:40	overcast	0° 90 °S 90 °N 60 °S 45 °N
20 August	Pineto	15:50–17:15	clear	0° 90 °W
22 August	Pineto	15:30–17:45	clear	0° 90 °E
23 August	Pineto	12:30–13:30	clear	0° 90 °N
		15:30–17:45	clear	0° 90 °N

The measurements were executed by means of Gigahertz-Optic, Munich, Germany, dosimeters: they provide on the same plane both UVA irradiance (W/m^2) and erythral irradiance (W/m^2). One measurement each minute was recorded. A support installed on an easel was used to place the instruments at 1.5 m from the ground facing the four orientations (N, E, S and W) with several inclinations: 0° (horizontal), 90° (vertical), 45° and 60°.

2.2. Calculation

The recorded data were extracted from the instruments and analyzed separately for each day of measurement and for each plane. The UVE ratio between erythral irradiance on an inclined plane (I_{ery}°) and UVA irradiance on a horizontal plane (IUVAh) was calculated for each minute recorded using the following equation:

$$UVE = I_{ery}^\circ / IUVAh, \quad (1)$$

The UVE did not have a constant value over time, but it varied during the interval of measurement. A UVEC curve was identified for each plane of measurement, which represented the variation in the UVE ratio as a function of the sun's position across the sky: it was designed by plotting in sequence the values of the UVE ratio against the cosine of the SZA.

The UVEC curves of planes with the same orientation and inclination referring to measurements of different days were analyzed together to identify a common trend for the specific plane. The UVEC curves were plotted in three graphs identified with similar sky conditions: clear sky, intermediate sky and overcast sky.

Successively, UVECc cosine curves were derived for each sky condition. Where a clear uniform trend was identifiable, the UVEC curves were joined to form a single UVECc curve, representing the trend of the $UVE = I_{ery}^\circ / IUVAh$ of the specific plane. When the UVEC curves had similar trends, the UVECc was derived from the mean UVE values of the available UVEC curves.

For each UVECc, the fitting curve was defined, and its equation was established: they represent the UVE models and their mathematical equations to calculate erythral exposure.

3. Results

3.1. UVE Ratio

The values of the UVE ratio calculated on each plane vary during the day: the maximum, mean and minimum values of the UVE calculated for each plane on all the measured days from one-minute results are reported in Appendix A.

In some cases, the value of the UVE ratio is higher than 1: this could be possible for some circumstances in which the value of the I_{ery}° is higher than the value of the IUVAh. It can occur when the horizontal plane is shaded, and the tilted plane is under the sun, or when the ground reflects a high amount of radiation to the tilted plane and nothing to the horizontal one.

The results of the calculations indicate that the value of the UVE depends on the inclination and orientation of the plane. For instance, for the plane 90° S, the value of the

UVE often ranged between 0.35 and 0.65; for the plane 90° E, it mostly ranged between 0.15 and 0.40; for the 60° N, it ranged between 0.35 and 0.70.

Considering the orientation of the planes, the UVE of the south orientation was generally higher than the UVE of the east and north orientations for the planes 90° and 60°, while for the 45° planes, the highest UVE was found for the north orientation. For the north and south orientations, the value of the UVE increased when the inclination of the planes decreased from 90° to 45°, while for the east and west orientations, the highest values of the UVE were calculated for planes at 60°.

The analysis of the UVE ratio indicated that its value depends on the orientation and inclination of the plane, but it seems scarcely related to the month and season; for this reason, the following analysis considered the UVEC curves grouped for orientation and inclination.

3.2. UVEC Curves

The UVEC curves were designed by plotting the values of the UVE ratio against the cosine of the SZA, so they represent the trend of the UVE with the sun's position in the sky for each plane.

Figures 1–3 show the trends of the UVEC related to the 90° planes, 60° planes and 45° planes oriented to the north.

The top graph of Figure 1 shows that the UVEC of the 90° planes in clear sky conditions, even if they are a little distant from each other, follow the trend of the 21 June curve: in this case, the value of UVE slightly increases from the intermediate to the high cosine values. Also, for the overcast condition, a clear trend emerges from the curves in the bottom graph, while the single curve in the middle graph does not provide enough information for the intermediate condition.

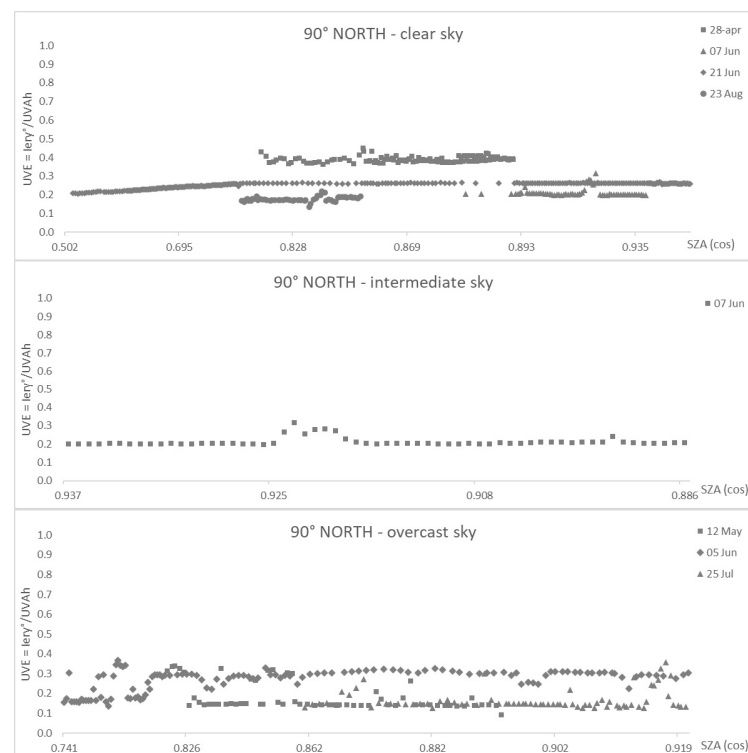


Figure 1. UVEC curves for the 90° plane oriented to the north: clear sky (**top**), intermediate (**middle**) and overcast (**bottom**) sky conditions.

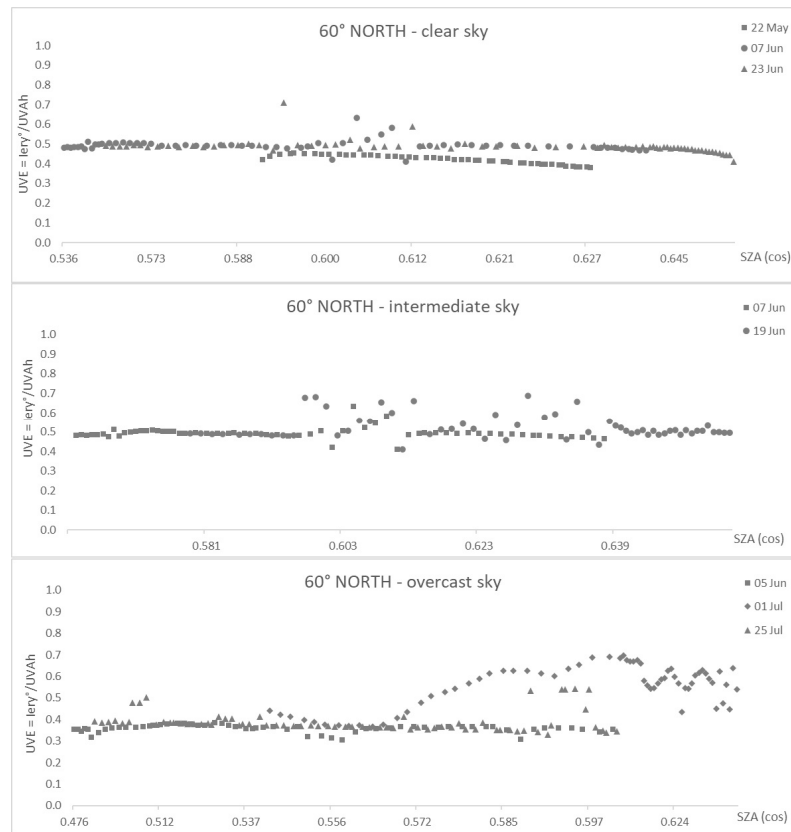


Figure 2. UVEC curves for the 60° plane oriented to the north: clear sky (top), intermediate (middle) and overcast (bottom) sky conditions.

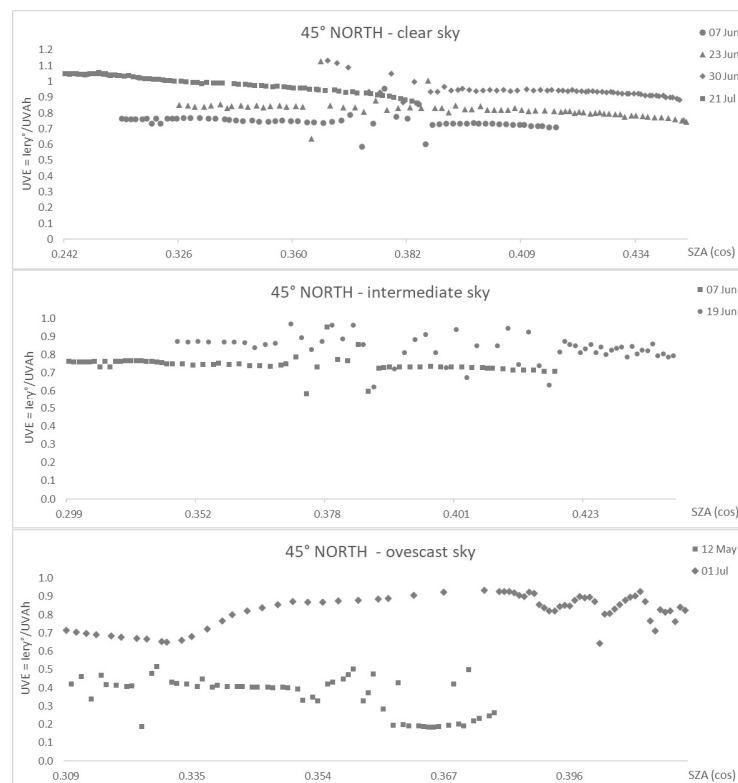


Figure 3. UVEC curves for the 45° plane oriented to the north: clear sky (top), intermediate (middle) and overcast (bottom) sky conditions.

The curves in the top graph of Figure 2 show a clear trend for the 60° plane in clear sky conditions: by joining the very close curves of 7 June and 23 June that partially overlap, it is possible to notice that the value of the UVE ratio slightly decreases with the increase in the cosine value. Also, for the covered sky condition, it is possible to identify a trend of the UVEC referred to on 5 June and 25 July.

The top graph of Figure 3 shows that the curves referring to the 45° north with clear sky have a similar trend that can be represented by 23 June; on the contrary, the few data samples presented in the middle and bottom graphs do not allow for the identification of a trend for the intermediate and overcast sky conditions.

The trends of the UVEC for the planes oriented to the south are shown in Figures 4–6: the top graphs refer to the clear sky, the middle graphs to the intermediate sky, and the bottom graphs to the overcast sky.

Analyzing the graphs of Figure 4, it is possible to identify similar trends of the UVEC for all weather conditions. For clear sky condition, it is possible to notice that the UVEC curves follow the trend of the 21 June curve: the values of the UVE ratio increase for the intermediate values of the cosine and then slowly decrease for the higher cosine values. The curves referring to the overcast and intermediate sky conditions also show a common linear trend for the high cosine values.

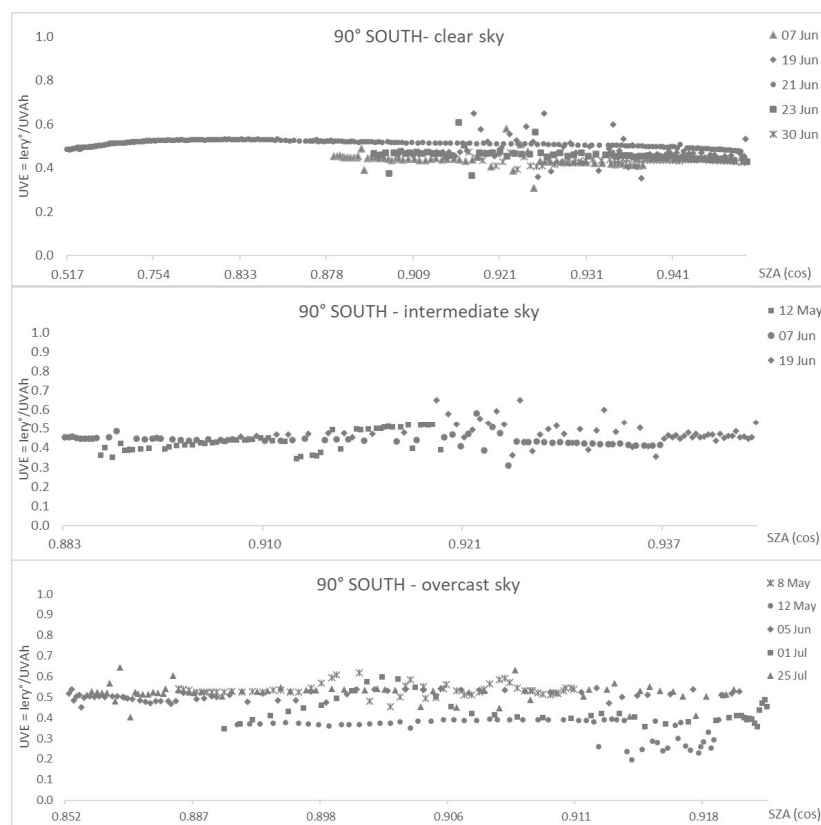


Figure 4. UVEC curves for the 90° planes oriented to the south: clear sky (top), intermediate (middle) and overcast (bottom) sky conditions.

The graphs in Figure 5 show a clear trend of the UVEC for the clear and intermediate sky conditions, while the data of the overcast sky are discordant. From the top graph, it is possible to see that the curves follow the trend of the 21 June UVEC, which increases from low to intermediate cosine values and then slowly decreases for the high cosine values. The trend in the middle graph is identifiable with the 7 June UVEC, to which the other data are close.

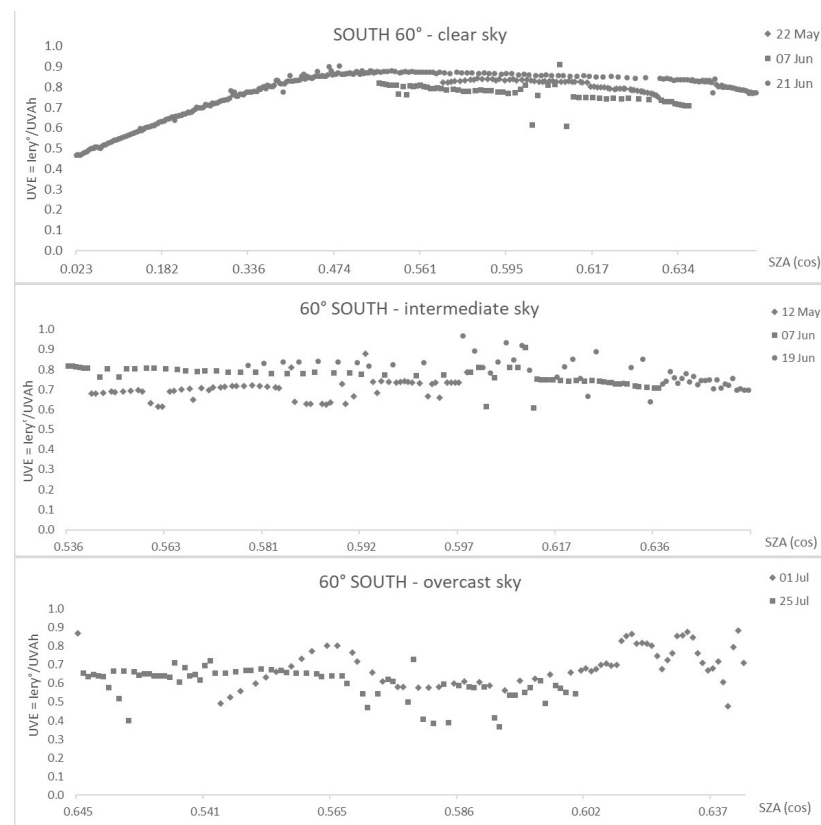


Figure 5. UVEC curves for the 60° planes oriented to the south: clear sky (**top**), intermediate (**middle**) and overcast (**bottom**) sky conditions.

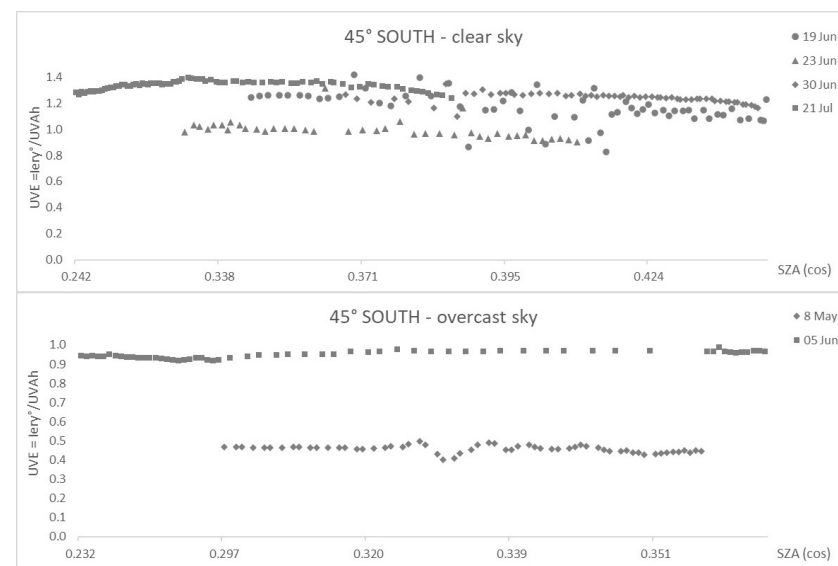


Figure 6. UVEC curves for the 45° planes oriented to the south: clear sky (**top**) and overcast (**bottom**) sky conditions.

For the 45° planes oriented to the south, only the graphs of clear and overcast sky conditions resulted from the measured data. The top graph shows that all the curves have a similar trend, and the UVE values slowly decrease from low to intermediate cosine values, while the two curves in the bottom graph are too distant to identify a common trend.

Figures 7 and 8 show the trends of the UVEC related to the planes oriented to the west: the measured data provide results for all three sky conditions only for the 90° planes, while

for the 60° and 45° planes, data were recorded in only one condition and the respective results are shown in the same figure.

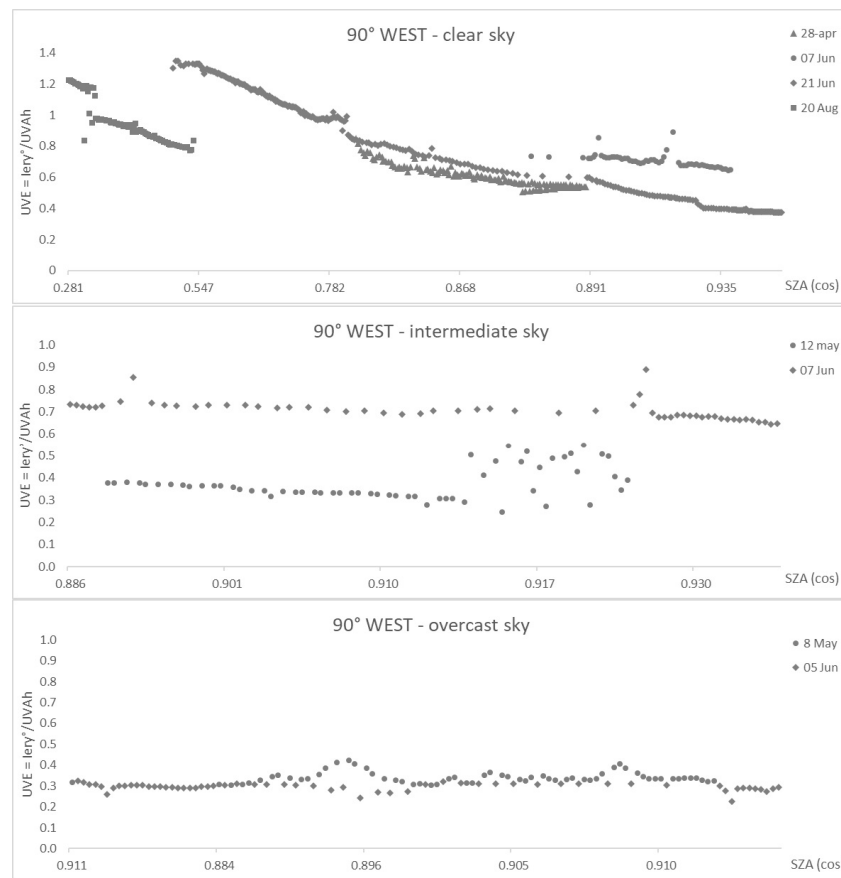


Figure 7. UVEC curves for the 90° planes oriented to the west: clear sky (top), intermediate (middle) and overcast (bottom) sky conditions.

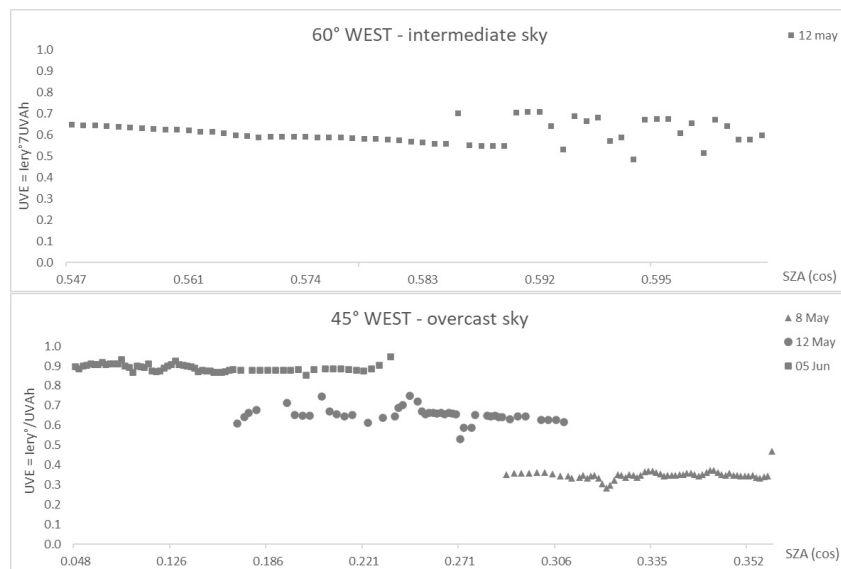


Figure 8. UVEC curves for the 60° and 45° planes oriented to the west: intermediate (top) and overcast (bottom) sky conditions.

For the west planes, the UVEC curves related to the vertical position in the clear sky conditions also follow the trend of the 21 June curve, with values decreasing from intermediate to high cosine values. A trend can also be identified for the overcast sky condition joining together the curves in the bottom graph of Figure 7, while the two curves of the middle graph do not allow us to derive a common trend.

Concerning Figure 8, the curves in the bottom graph indicate a decreasing trend of the UVE values from the first to the intermediate cosine values for the 45° planes in overcast sky conditions, while the single curve in the top graph does not give sufficient information to deduce a trend for the 60° planes in intermediate sky conditions.

Figures 9 and 10 show the trends of the UVEC oriented to the east: for this orientation, the measured data provides results for all three sky conditions only for the 90° planes, while for the 60° and 45° planes, data were recorded only in two conditions and the respective results are shown in the same figure.

The data for the 90° planes with east orientation produced curves slightly distant from each other but with a clear trend for the clear sky as well as for the overcast sky. In the first case, the UVEC trend can be identified with that of the 21 June curve, whose values increase from low to high cosine values; in the second case, the UVE values remain almost constant, and a mean trend can be derived. The single curve in the middle graph of Figure 9 does not provide sufficient data to define a trend for intermediate sky conditions.

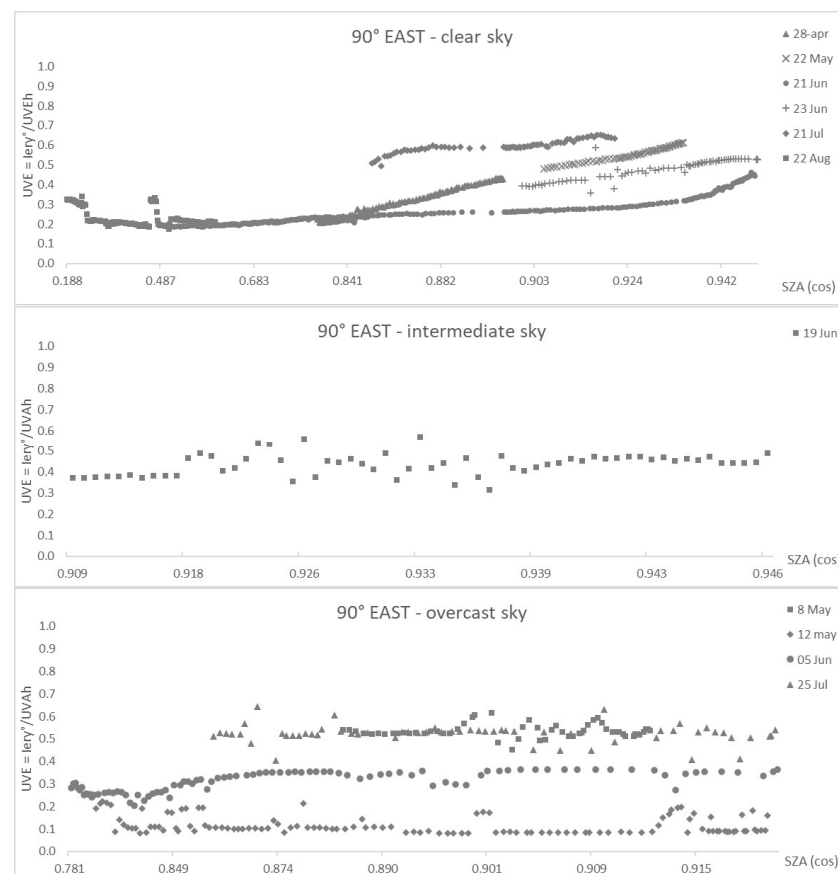


Figure 9. UVEC curves for the 90° planes oriented to the east: clear sky (**top**), intermediate (**middle**) and overcast (**bottom**) sky conditions.

Regarding the 60° planes oriented to the east, the only condition for which it is possible to identify a trend is the overcast sky condition: the middle graph of Figure 10 shows that the values of the UVEC gradually increase from low to high cosine values. The single curve in the top graph of Figure 10, referring to the 60° plane, seems to follow the same trend of the 90° UVEC, but the data available are not sufficient to define a trend for the clear sky

condition; also, the single curve referring to the 45° plane does not allow us to identify a trend for the intermediate sky condition.

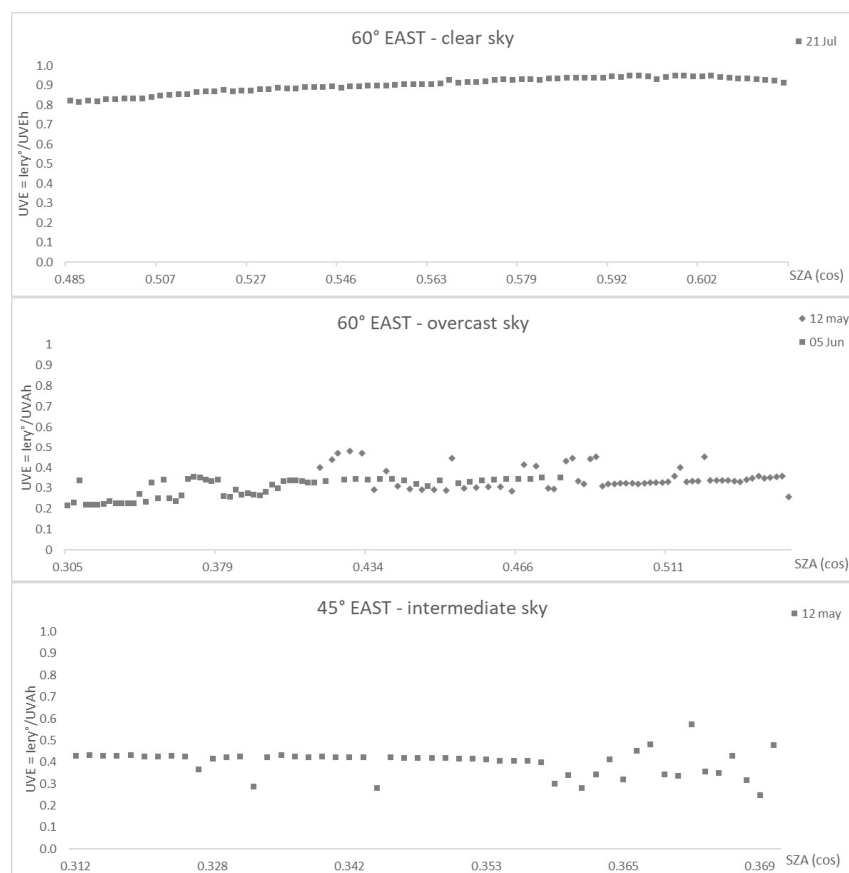


Figure 10. UVEC curves for the 60° and 45° planes oriented to the east: clear sky (**top**), overcast (**middle**) and intermediate (**bottom**) sky conditions.

3.3. UVE Mathematical Models

In order to obtain mathematical models describing the distribution of the UVE ratio according to the sun's position in the sky, UVEC cosine curves, representative of the UVE trend in function of the cosine of the SZA were defined for each plane in the different sky conditions. The fitting curves of the UVEC represent the UVE models, and their equations are their mathematical expressions.

The UVE models for the 90°, 60° and 45° planes oriented to the north are shown in Figure 11 together with their UVEC generative curves. The clear sky UVEC of the 90° plane corresponds to the UVEC of 21 June, and the clear sky UVEC of the 45° plane corresponds to the 23 June UVEC, since both have a clear trend and the other UVEC curves are very close to them. Moreover, they can be considered valid models because they also approximate very well with the overcast sky models. The UVEC of the 60° plane was generated by interpolating the values of the 7 June and 23 June UVEC curves; also, in this case, the UVEC is very close to the other UVEC curves for the same plane. The UVEC curves for the north orientation in overcast sky conditions were defined by calculating the mean values of the UVEC for the respective planes. All the other UVE models were not defined since the data available did not give enough information.

The UVE models for the south orientation and their UVEC generative curves are shown in Figure 12. The UVEC for the 90° and 60° planes in clear sky conditions correspond to the respective 21 June UVEC curves, while that of the 45° plane was defined joining the curve of 30 June with the adjacent curve of 21 July that continues its trend. The

other UVEC curves approximate these UVECc curves, so all these UVE models can also be considered valid for them.

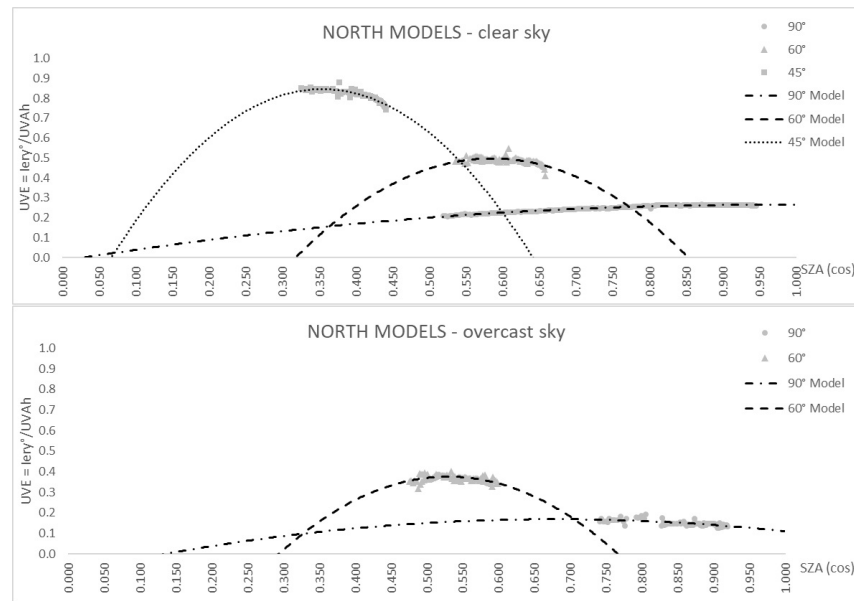


Figure 11. UVECc and UVE models of the 90°, 60° and 45° planes for the north orientation: clear sky models (top) and overcast sky models (bottom).

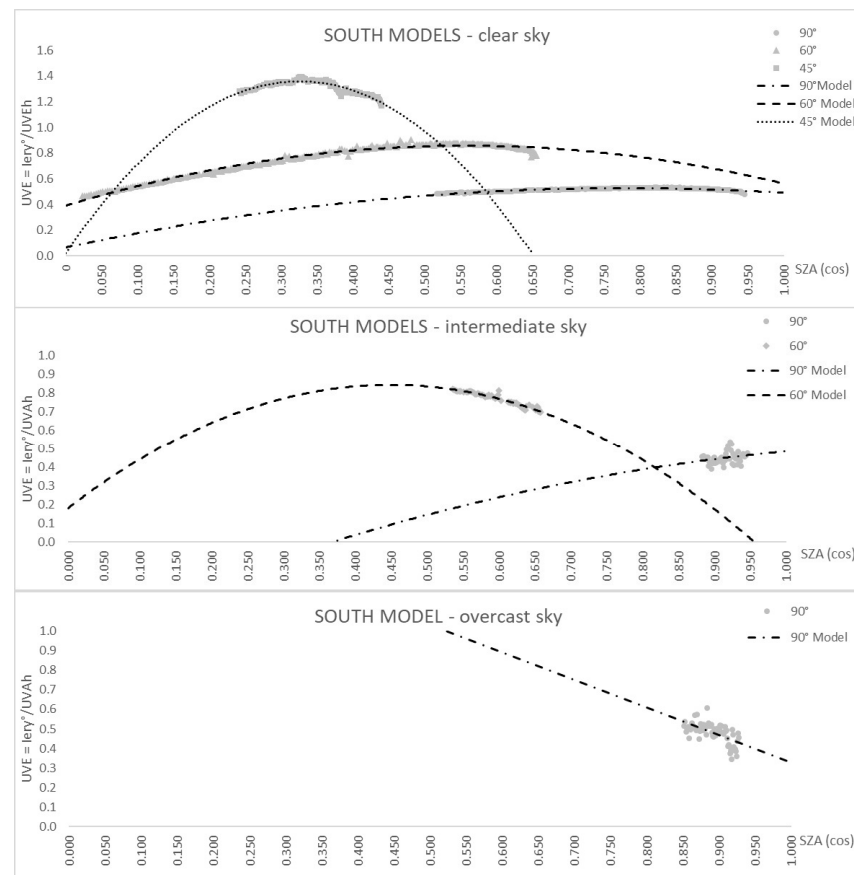


Figure 12. UVECc and UVE models of the 90°, 60° and 45° planes for the south orientation: clear sky models (top), intermediate sky models (middle) and overcast sky models (bottom).

The 90° UVECC values for both the intermediate and the clear sky conditions were defined calculating the mean values of the UVEC curves for each cosine value, while the 60° UVECC for the intermediate sky corresponds to the 7 June curve to which the other UVEC curves closely approximate. No UVE models could be established for the other planes since the data were not sufficient to define any UVECC curve.

Figure 13 shows the UVE models of the 90° and 45° planes oriented to the west together with the respective UVECC; no model could be defined for the 60° plane to the west since the data were not sufficient. The UVECC of the clear sky for the 90° plane corresponds to the UVEC of 21 June: it has a clear trend, and the other UVECs are very close to it. The UVECC for the cloudy sky condition was defined joining together the UVEC of the 45° plane: the single UVEC curves were one consequent to the other and all together defined a trend.

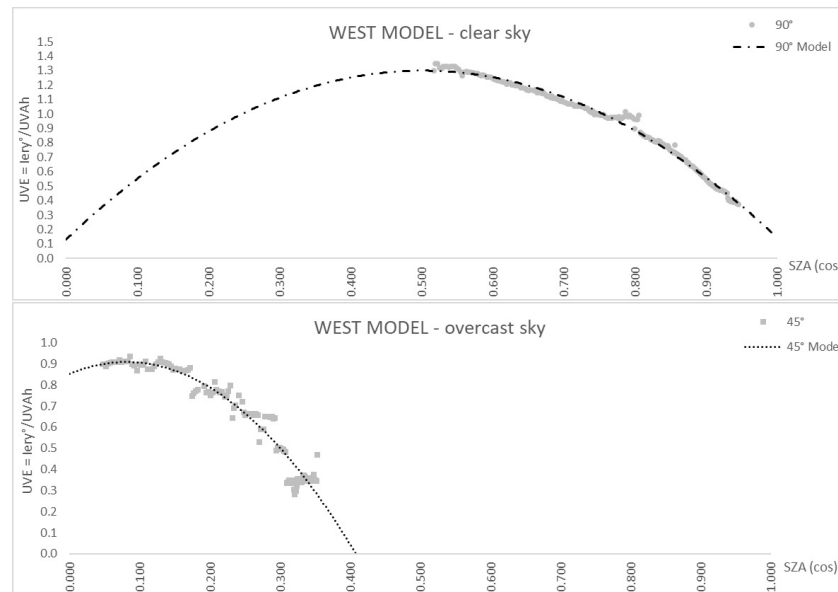


Figure 13. UVECC and UVE models of the 90° and 45° planes for the west orientation: clear sky model (top) and overcast sky model (bottom).

Figure 14 shows the 90° and 60° models for the east orientation; no models could be defined for the 45° planes due to the scarce amount of data available. Also, in this case, the clear sky model for the 90° plane corresponds to the UVEC of 21 June: the other UVEC curves for clear sky conditions are very close to it. Both the 90° and 60° UVECC curves of the overcast sky were obtained from the mean values of the respective UVEC curves, which all have similar trends.

For each UVE model, the respective equation was defined; the mathematical equations that describe the UVE models are reported in Table 2.

Table 2. Equations describing the UVE models of the different planes.

Plane	Clear Sky	Intermediate Sky	Overcast Sky
90° N	$y = -3 \times 10^{-7}x^2 + 0.0006x - 0.0176$		$y = -6 \times 10^{-7}x^2 + 0.0008x - 0.0945$
60° N	$y = -7 \times 10^{-6}x^2 + 0.0081x - 1.893$		$y = -7 \times 10^{-6}x^2 + 0.0071x - 1.5175$
45° N	$y = -10^{-5}x^2 + 0.0073x - 0.4471$		
90° S	$y = -8 \times 10^{-7}x^2 + 0.0012x + 0.0641$	$y = -7 \times 10^{-7}x^2 + 0.0017x - 0.5218$	$y = -0.0014x + 1.7356$
60° S	$y = -2 \times 10^{-6}x^2 + 0.0017x + 0.3894$	$y = -3 \times 10^{-6}x^2 + 0.003x + 0.1776$	
45° S	$y = -10^{-5}x^2 + 0.0083x + 0.01$		
90° W	$y = -5 \times 10^{-6}x^2 + 0.0047x + 0.1277$		
45° W			$y = -8 \times 10^{-6}x^2 + 0.0014x + 0.8516$
90° E	$y = 7 \times 10^{-7}x^2 - 0.0007x + 0.3691$		$y = 0.1325 \times 10^{0.0019x}$
60° E			$y = 0.0238 \times 10^{0.0029x}$

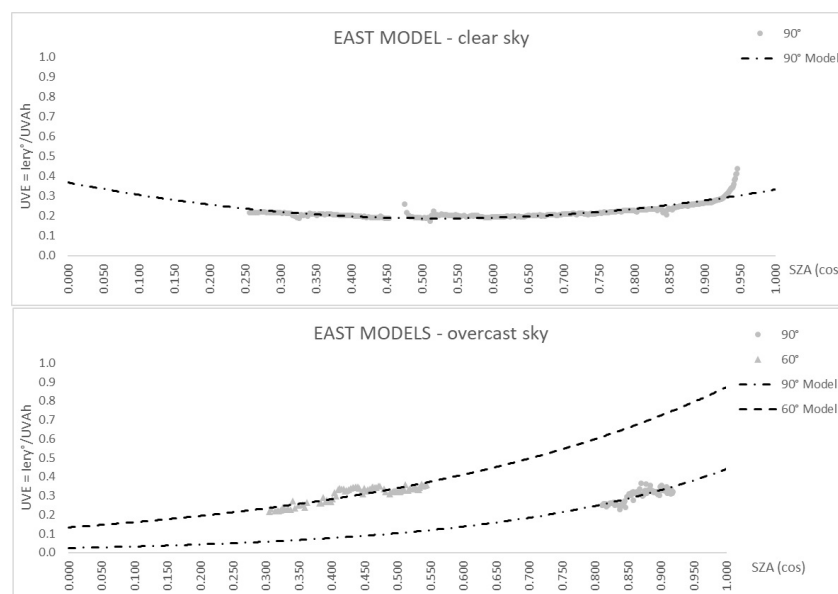


Figure 14. UVEc and UVE models of the 90° and 60° planes for the east orientation: clear sky model (top) and overcast sky model (bottom).

The equations of the UVE models for the north, south and west planes are all polynomials of the second order, representing parabolas with downward concavity, with the exception of the 90° plane oriented to the south in overcast sky conditions, which is a straight line with negative inclination. In these models, the values of the UVE ratio increase at low or intermediate cosine values, reach a maximum and then decrease for intermediate or high cosine values.

The equations describing the east models are exponentials representing curves having upward concavity, in which the UVE values slightly increase from low to high cosine values. Only the model of the 90° in clear sky conditions is a polynomial of the second order with an upward concavity that represents a flat parabola.

3.4. Application of the UVE Models

Using the UVE models, it is possible to derive the erythemal exposure of a defined plane located in any environmental context in which the horizontal UVA irradiance is known.

The procedure starts with the identification of the inclination and orientation of the plane and the weather conditions. Hypothesizing, for example, a plane oriented to the south, in vertical position (90°), during a clear-sky day, the UVE model that describes its exposure is expressed with the equation $y = -8 \times 10^{-7}x^2 + 0.0012x + 0.0641$ (see Table 2).

To apply the model, at least one measure of the horizontal UVA irradiance measured in the same place of the exposed plane during the exposure time is required. The satellite data of IUVAh or the value provided by the nearest weather station could be used too, but this would decrease the precision of the result. On the contrary, using more than one value measured within the exposure time would increase the precision of the calculation result. In this example, the exposure occurred on the 21 of July from 12:30 to 14:00 and the IUVAh was measured every 10 min.

The x values of the models correspond to the cosine values of the SZA in the exposure interval multiplied by the absolute number 1000, i.e., $x = \cos(\text{SZA}) \times 1000$. Applying the correct value of x in the equation model, the corresponding y value can be calculated: this value is the UVE ratio. In this example, for $x = 925$, the UVE is 0.490, and for $x = 845$, the UVE is 0.507.

Multiplying the IUVAh for the corresponding UVE value, the erythemal irradiance on the plane can be calculated. In Table 3, the resulting values of erythemal irradiance (I_{ery}) together with the measured values of IUVAh and the UVE ratio, were reported every 10 min in the exposure period 12:30–14:00 as an exemplum.

Table 3. Results of erythemal irradiance and the corresponding values used in the calculation procedure.

Hour (hh:mm)	x	UVE	IUVAh (W/m ²)	I_{ery} (W/m ²)
12:30	925	0.490	0.0257	0.01257
12:40	921	0.491	0.0258	0.01264
12:50	916	0.492	0.0261	0.01285
13:00	910	0.494	0.0264	0.01304
13:10	902	0.496	0.0265	0.01316
13:20	893	0.498	0.0266	0.01323
13:30	883	0.500	0.0265	0.01325
13:40	871	0.502	0.0265	0.01333
13:50	858	0.505	0.0267	0.01349
14:00	845	0.507	0.0267	0.01354

The erythemal exposure E_{ery} can be finally calculated by multiplying the I_{ery} for the exposure interval of time in seconds. Considering the exposure period 12:30–14:00, the corresponding E_{ery} is 78.665 J/m² if the values of I_{ery} are available each minute or even every 10 min, as in the exemplum; less precise values of erythemal exposure can be calculated with a lower amount of erythemal irradiance data. If only one value of I_{ery} is available, for instance, at the hour 12:30, it must be multiplied for the whole time interval of 5400 s to calculate the corresponding E_{ery} ; in the second case, the resulting E_{ery} is 67.877 J/m².

4. Discussion

The results concerning the calculation of the UVE ratio show that, for all the measured planes, its value is not constant during the interval of measurement, but it is variable with the position of the sun in the sky and the values assumed by the UVE form curves (UVEC). In fact, the two values of IUVAh and I_{ery} differ with the SZA and its ratio is variable with the cosine of the SZA.

The results of the analysis show that the trend of the UVEC depends on the plane orientation and inclination. Curves referring to the same day have different trends, since the I_{ery} varies according to the inclination degree of the plane and with its orientation, while the values of the IUVAh are related to the horizontal plane. Moreover, the UVEC trends depend on sky conditions: the amounts of direct and diffuse UV radiation differ in intermediate and overcast skies with respect to clear sky, and, consequently, the percentage of irradiation of the different planes differs with sky coverage. With a clear sky, the direct radiation from the sun is predominant and additional diffuse radiation comes from the sky vault; in this sky condition, the higher irradiation level on the Earth is generally registered. When the clouds completely cover the sky vault, the direct radiation from the sun is shaded and only a limited percentage crosses the clouds as diffuse radiation; therefore, in the overcast sky condition, a lower amount of irradiation is generally measured on the ground. During intermediate sky conditions, the sun and the sky are partially shaded from the clouds: only a portion of the sky vault is visible and sometimes also the sun's rays go beyond the clouds. These are the most variable conditions in which direct and diffuse radiation can be present, but both are normally attenuated by the clouds. In intermediate sky conditions,

a higher irradiation level can be registered on Earth, due to interreflections of the sunrays within the clouds that amplify the irradiation level registered on the ground [26]. This means that the daily trends of both the IUVAh and the I_{ery}° in overcast and intermediate sky conditions are not the same as those with clear sky conditions.

The many measurements executed during the year, in several environments and under different weather conditions, indicated that all the UVEC values referring to the same planes and weather conditions have a similar trend. Even if the UVE is not constant during the day, the UVEC trend is repeated for the same SZA. The figures from 1 to 10 show that the UVEC curves referred to different days, even in different seasons, have similar trends; for instance, Figure 7 shows that the UVEC results referring to 28 April and 21 June for the same plane (90° west) have the same trend

Similarly, the environment in which the measurements were executed did not have a significant influence on the UVEC trend. It is possible to notice in Figure 4, for the plane 90° south and overcast sky conditions, that the UVEC of 5 May referring to the park of Ancient Appia is overlapped with the UVEC of 8 May referring to the terrace and to the UVEC of 25 July referring to the marble staircase. Another example with intermediate sky conditions is shown in Figure 4 (90° south), where the UVEC of 12 May relating to the city square is overlapped with the UVEC of 7 June (park of Ancient Appia).

The similarities of the UVEC curves previously described allowed us to derive UVE models referring to planes with the same orientation and inclination, for the three sky conditions. Figures 11–14 show that the trend of the UVE model mainly depends on the orientation, and in some cases, on the weather conditions, while the plane inclination influences the curvature: Figures 11 and 12 clearly show that the UVE models of the 90° planes are flatter than those of the 60° and 45° planes.

All the UVE models are parabolas, except for the east orientation, for which two UVE models are exponential curves (Figure 14) and the south model in overcast sky conditions that is a straight line (Figure 12). The concavity of the UVE models differs with the orientation: it is downward for the north, east and south planes, while it is upward for the east planes. Moreover, the east UVE models have an opposite trend with respect to the other models, which generally reach their maximum for intermediate cosine value, and the models of the east planes have their minimum in the low or intermediate cosine values.

The different trends of the UVE models are due to the sun's position during the day: when the inclined plane is exposed to the sun, the $UVE = I_{ery}^\circ / IUVAh$ is higher than when the inclined plane is shaded. For this reason, the value of the UVE ratio is higher in the morning than in the afternoon for the east planes, while for the west planes, it is higher in the afternoon than in the morning. Theoretically, the I_{ery}° can also be derived from the erythemal irradiance on the horizontal plane by applying the geometrical rule based on the ratio of the two SZA cosines [59]; practically, it does not consider the shading due to the orientation of the plane and this would lead to a relevant error in the calculation of erythemal exposure. The horizontal erythemal irradiance must be measured with scientific instruments, while the UVAh is easily accessible since it is provided by environmental stations and satellites: for this reason, this study used the UVAh.

The UVE mathematical models are described by polynomial equations of the second order for most of the planes and by exponential equations for the two west planes. The equations indicate that the polynomial curves of the 90° planes are very flat, having more decimal numbers at the squared terms, while those referring to the 60° and 45° planes are less flat. The equations also indicate that at the increase in the plane angle, the UVE model curve is positioned corresponding to the lower values of the UVE coefficient: the first graphs of Figures 11 and 12 show that the UVE model curves of the 90° planes are placed under those of the 60° planes, which are placed under the UVE model curves of the 45° planes.

5. Conclusions

The obtained results demonstrate that it is possible to define a relationship between UVA solar irradiance on the horizontal plane (IUVAh) and erythemal irradiance referring to planes with different orientations and inclinations (I_{ery}°): this relationship is expressed as a ratio named UVE. As expected, this UVE ratio differs according to the orientation and inclination of the plane and the weather conditions; moreover, it is variable during the day, since the ratio between the I_{ery}° and the IUVAh depends on the sun's position and the level of shading of the considered plane. For this reason, the relationship between the I_{ery}° and the IUVAh is defined by hourly UVEC curves, generally having a parabolic shape. The I_{ery}° cannot be derived from the IUVAh using simple geometrical and diffuse models, since erythemal irradiance derives from solar irradiance through a weighting process with an action spectrum and an integration process instead of a simple coefficient that is requested to pass from solar irradiance to erythemal irradiance.

From the many measurements executed during the year in different weather conditions, UVE models of clear sky and cloudy sky conditions were derived for 90° , 60° , and 45° planes in the four cardinal directions, valid for all the seasons and in several environments.

As explained in the applicative example, using the UVE models, the erythemal exposure E_{ery} on the body districts can be easily calculated with a few simple passages by automatic systems, without measuring the spectral UV irradiance and without post-processing the data with the action spectrum curve. Applying the UVE mathematical model, it is possible to derive the value of the UVE ratio related to a specific plane at any hour of any day. Using the UVE, it is possible to easily calculate the value of erythemal irradiance on a plane starting from the value of the horizontal solar UVA irradiance level. By multiplying the values of erythemal irradiance for the exposure time, it is finally possible to calculate the erythemal exposure. Alternatively, forecasting the values of erythemal exposure in the following hours of the day is also possible.

Respect to previous studies [49,50,54], the models defined in this work do not provide the UVI, which is an index indicating the dangerousness of UV solar radiation, but they do calculate erythemal exposure that is a quantity related to erythemal damage: for instance, once the MED threshold dose established for the skin type is exceeded, erythema occurs on the skin. Moreover, the models presented in this work expand on the literature that assesses erythemal exposure on the horizontal plane [57,58], providing the equations to calculate erythemal exposure on several inclined planes in the four cardinal directions; the inclined planes approximate the exposure of many body districts, such as the face, the chest, the back and the limbs, better than the horizontal plane that can estimate the exposure of the shoulders and the feet.

With respect to other models that can predict the exposure of body districts considering clothing coverage or vacation habits [66,67], the models presented in this study have a more general valence: they can be applied to all the exposed body parts (with clothing they are not exposed) and to whichever behavior. They are not based on forecasted UV values or linear regression models [53,65], but they were defined starting from instrumental measurements that allow for the consideration of the modifications due to weather conditions; moreover, the application of these models is not limited to a specific region [55,56], since they are defined as a function of the cosine of the SZA, so the erythemal exposure can be calculated knowing the sun's position in the sky.

This work has some limitations. Despite the many measurements executed, for some planes, the data were not sufficient to elaborate the UVE model; moreover, only three inclinations and the four principal cardinal directions were investigated. Models for other inclinations and other orientations would also be needed for a practical application. Even when the UVE model could be defined, the limited amount of data did not allow us to validate them. The measurement campaign included several different environments, but other locations could be investigated to confirm that the surroundings do not impact the models, in particular, if the environment is characterized by high albedo values. Also, some data should be recorded in winter, to confirm the validity of the model for the whole year.

Probably the most important limitation is that in many cases, the measurements covered a temporal arc of one hour, and for this reason, some models were defined joining adjacent curves. Moreover, the data before 11:00 are completely missing. In a large part of the year, the relevant hours for the erythemal damage range from 11:00 to 15:00.

A larger measurement campaign will be carried out in future work, which will include many planes and orientations, many environments and days, and recording periods covering almost three hours, to confirm the trends of the UVE models. Some measurements will also include the early morning hours, in particular for the west planes. A more consistent measurement campaign is needed to validate the models: the present study is a starting point and a reference for a larger-scale study.

Author Contributions: Conceptualization, F.B. and M.B.; methodology, C.B.; validation, C.B. and F.V.; formal analysis, C.B.; investigation, C.B. and F.V.; data curation, C.B.; writing—original draft preparation, C.B.; writing—review and editing, C.B.; visualization, F.V. and M.B.; supervision, F.B.; project administration, F.B.; funding acquisition, F.B. All authors have read and agreed to the published version of the manuscript.

Funding: This research was funded by Italian Workers Compensation Authority (INAIL), grant number BRIC 2019 ID 08.

Data Availability Statement: The raw data supporting the conclusions of this article will be made available by the authors on request.

Conflicts of Interest: The authors declare no conflicts of interest.

Appendix A

The following Table A1 reports the maximum, mean and minimum values of the UVE calculated for each plane on all the measured days from one-minute results.

Table A1. Values of the UVE ratio.

Day	Hours	Planes	UVE Min	UVE Mean	UVE Max
28 April	11:35–13:40	90° E	0.21	0.34	0.47
		90° W	0.51	0.61	0.85
		90° N	0.36	0.39	0.45
8 May	11:00–12:00	90° S	0.45	0.54	0.62
		90° E	0.15	0.19	0.24
		45° S	0.40	0.46	0.50
	12:00–13:00	90° W	0.30	0.34	0.42
		90° S	0.23	0.29	0.38
		45° W	0.28	0.35	0.47
12 May	11:00–12:00	90° W	0.25	0.37	0.55
		90° S	0.20	0.35	0.39
		60° W	0.48	0.61	0.71
		45° E	0.25	0.45	0.57
	12:00–13:00	90° S	0.34	0.44	0.52
		90° E	0.08	0.11	0.20
		60° S	0.62	0.70	0.88
		45° N	0.19	0.37	0.52
13:00–14:00	13:00–14:00	90° E	0.08	0.13	0.22
		90° N	0.09	0.18	0.34
		60° E	0.26	0.35	0.48
		45° W	0.53	0.65	0.75
		90° S	0.48	0.55	0.61
22 May	11:00–12:00	90° N	0.46	0.50	0.52
		60° N	0.27	0.40	0.46
		60° S	0.75	0.81	0.84
		60° S	0.75	0.81	0.84

Table A1. Cont.

Day	Hours	Planes	UVE Min	UVE Mean	UVE Max
5 June	13:00–14:00	90° S	0.45	0.51	0.55
		90° E	0.27	0.34	0.37
		90° W	0.22	0.30	0.35
		90° N	0.23	0.30	0.33
		60° N	0.31	0.36	0.38
	14:00–15:00	45° S	0.92	0.95	0.99
		90° S	0.24	0.45	0.62
		90° E	0.14	0.21	0.31
		90° W	0.23	0.42	0.54
		90° N	0.14	0.24	0.37
7 June	11:30–12:30	60° E	0.21	0.30	0.35
		45° W	0.85	0.89	0.93
		90° S	0.31	0.44	0.58
		90° W	0.65	0.71	0.89
		90° N	0.20	0.21	0.32
		60° S	0.61	0.77	1.00
19 June	11:20–12:20	60° N	0.41	0.49	0.63
		45° N	0.59	0.75	0.95
		90° S	0.35	0.48	0.65
		90° E	0.32	0.44	0.57
		60° S	0.64	0.78	0.97
21 June	12:00–16:30	60° N	0.41	0.52	0.69
		45° N	0.62	0.84	0.97
		90° S	0.46	0.51	0.53
		90° E	0.18	0.26	0.47
		90° N	0.21	0.25	0.27
23 June	11:20–12:20	90° W	0.37	0.81	1.35
		60° S	0.47	0.76	1.02
		90° S	0.46	0.51	0.53
		90° E	0.36	0.48	0.59
		60° N	0.41	0.49	0.71
30 June	12:10–13:10	45° N	0.64	0.82	1.13
		90° S	0.39	0.43	0.47
		60° S	0.54	0.61	0.67
1 July	12:30–13:30	45° N	0.87	0.94	1.13
		90° S	0.25	0.42	0.63
		90° N	0.54	0.61	0.67
		60° S	0.48	0.72	0.89
		60° N	0.37	0.55	0.70
21 July	12:30–13–50	45° N	0.64	0.82	0.93
		90° E	0.49	0.60	0.65
		60° S	0.81	0.90	0.95
		60° N	0.33	0.40	0.65
25 July	11:30–12:40	45° N	0.86	0.99	1.06
		90° S	0.18	0.52	0.97
		90° N	0.13	0.17	0.36
		60° S	0.40	0.52	0.64
20 August	15:50–17:15	60° N	0.33	0.39	0.54
22 August	15:30–17:45	90° W	0.77	0.95	1.23
23 August	12:30–13:30	90° E	0.18	0.23	0.34
	15:30–17:45	90° N	0.14	0.18	0.22
		90° N	0.27	0.42	0.57

References

1. Lucas, R. *Solar Ultraviolet Radiation: Assessing the Environmental Burden of Disease at National and Local Levels*; Environmental Burden of Disease Series; No. 17; Prüss-Ustün, A., Perkins van Deventer, E., Eds.; World Health Organization: Geneva, Switzerland, 2010.
2. D’Orazio, J.; Jarrett, S.; Amaro-Ortiz, A.; Scott, T. UV radiation and the skin. *Int. J. Mol. Sci.* **2013**, *14*, 12222–12248. [CrossRef] [PubMed]
3. Chawda, D.; Shinde, P. Effects of Solar Radiation on the Eyes. *Cureus* **2022**, *14*, e30857. [CrossRef] [PubMed]
4. Gallagher, R.P.; Lee, T.K. Adverse effects of ultraviolet radiation: A brief review. *Prog. Biophys. Mol. Biol.* **2006**, *92*, 119–131. [CrossRef]
5. World Health Organization. Available online: <https://www.who.int/news-room/fact-sheets/detail/ultraviolet-radiation#:~:text=Excessive%20exposure%20to%20UVR%20caused,skin%20in%20the%20year%202020> (accessed on 17 July 2024).
6. Commission Internationale de l’Eclairage. *Erythema Reference Action Spectrum and Standard Erythema Dose*; CIE S007/E; Commission Internationale de l’Eclairage: Vienna, Austria, 1998.
7. Commission Internationale de l’Eclairage. *Rationalizing Nomenclature for UV Doses and Effects on Humans*; CIE TR 209; Commission Internationale de l’Eclairage: Vienna, Austria, 2014.
8. World Health Organization. *Global Solar UV Index: A Practical Guide*; World Health Organization: Geneva, Switzerland, 2002.
9. International Commission on Non-Ionizing Radiation Protection. ICNIRP statement—Protection of workers against ultraviolet radiation. *Health Phys.* **2010**, *99*, 66–87. [CrossRef]
10. Schmalwieser, A.W.; Casale, G.R.; Cosimo, A.; Schmalwieser, S.S.; Siani, A.M. Review on Occupational Personal Solar UV Exposure Measurements. *Atmosphere* **2021**, *12*, 142. [CrossRef]
11. Linde, K.; Wright, C.Y.; du Plessis, J.L. Personal Solar Ultraviolet Radiation Exposure of Farmworkers: Seasonal and Anatomical Differences Suggest Prevention Measures Are Required. *Ann. Work Expo. Health* **2022**, *66*, 41–51. [CrossRef]
12. Burattini, C.; Pompei, L.; Modenese, A.; Salvadori, G.; Militello, A.; Leccese, F.; Borra, M.; Gobba, F.; Bisegna, F. UV solar exposure of outdoor workers in Mediterranean area. In Proceedings of the 21st IEEE International Conference on Environment and Electrical Engineering and 2021 5th IEEE Industrial and Commercial Power System Europe, IEEEIC/I and CPS Europe 2021, Bari, Italy, 7–10 September 2021; Code 176982. [CrossRef]
13. Wittlich, M.; John, S.M.; Tiplica, G.S.; Sălăvăstru, C.M.; Butacu, A.I.; Modenese, A.; Paolucci, V.; D’Hauw, G.; Gobba, F.; Sartorelli, P.; et al. Personal solar ultraviolet radiation dosimetry in an occupational setting across Europe. *J. Eur. Acad. Dermatol. Venereol.* **2020**, *34*, 1835–1841. [CrossRef]
14. Modenese, A.; Bisegna, F.; Borra, M.; Burattini, C.; Gugliermetti, L.; Larese Filon, F.; Militello, A.; Toffanin, P.; Gobba, F. Occupational Exposure to Solar UV Radiation in a Group of Dock-workers in North-East Italy. In Proceedings of the 2020 IEEE International Conference on Environment and Electrical Engineering and 2020 IEEE Industrial and Commercial Power Systems Europe, IEEEIC/I and CPS Europe 2020, Madrid, Spain, 9–12 June 2020; p. 9160703.
15. Kovačić, J.; Wittlich, M.; John, S.M.; Macan, J. Personal ultraviolet radiation dosimetry and its relationship with environmental data: A longitudinal pilot study in Croatian construction workers. *J. Photochem. Photobiol. B* **2020**, *207*, 111866. [CrossRef]
16. Modenese, A.; Ruggieri, F.P.; Bisegna, F.; Borra, M.; Burattini, C.; Della Vecchia, E.; Grandi, C.; Grasso, A.; Gugliermetti, L.; Manini, M.; et al. Occupational Exposure to Solar UV Radiation of a Group of Fishermen Working in the Italian North Adriatic Sea. *Int. J. Environ. Res. Public Health* **2019**, *16*, 3001. [CrossRef]
17. Modenese, A.; Korpinen, L.; Gobba, F. Solar radiation exposure and outdoor work: An underestimated occupational risk. *Int. J. Environ. Res. Public Health* **2018**, *15*, 2063. [CrossRef]
18. Kutal, G.; Kolhe, A.; Varpe, S.; Mahajan, C.; Singh, P.; Aher, G. UV Erythematous Radiation and Its Sensitivity to Changes in Total Column Ozone and Aerosols. *Aerosol Sci. Eng.* **2022**, *6*, 176–185. [CrossRef]
19. Becerra-Rondón, A.; Ducati, J.; Haag, R. Spatiotemporal distributions of ultraviolet radiation from OMI orbital data and relationships with total O₃ and total NO₂. *Atmósfera* **2023**, *37*, 311–334. [CrossRef]
20. Chubarova, N.E.; Pastukhova, A.S.; Zhdanova, E.Y.; Volpert, E.V.; Smyshlyaev, S.P.; Galin, V.Y. Effects of ozone and clouds on temporal variability of surface UV radiation and UV resources over Northern Eurasia derived from measurements and modeling. *Atmosphere* **2020**, *11*, 59. [CrossRef]
21. Campanelli, M.; Diémoz, H.; Siani, A.M.; di Sarra, A.; Iannarelli, A.M.; Kudo, R.; Fasano, G.; Casasanta, G.; Tofful, L.; Cacciani, M.; et al. Aerosol optical characteristics in the urban area of Rome, Italy, and their impact on the UV index. *Atmos. Meas. Tech.* **2022**, *15*, 1171–1183. [CrossRef]
22. Kazadzis, S.; Raptis, P.; Kouremeti, N.; Amiridis, V.; Arola, A.; Gerasopoulos, E.; Schuster, G.L. Aerosol absorption retrieval at ultraviolet wavelengths in a complex environment. *Atmos. Meas. Tech.* **2016**, *9*, 5997–6011. [CrossRef]
23. Antón, M.; Gil, J.E.; Fernández-Gálvez, J.; Lyamani, H.; Valenzuela, A.; Foyo-Moreno, I.; Olmo, F.J.; Alados-Arboledas, L. Evaluation of the aerosol forcing efficiency in the UV erythematous range at Granada, Spain. *J. Geophys. Res.* **2011**, *116*, D20214. [CrossRef]
24. Kim, J.; Lee, Y.G.; Koo, J.-H.; Lee, H. Relative Contributions of Clouds and Aerosols to Surface Erythematous UV and Global Horizontal Irradiance in Korea. *Energies* **2020**, *13*, 1504. [CrossRef]
25. Calbó, J.; Pagès, D.; González, J.-A. Empirical studies of cloud effects on UV radiation: A review. *Rev. Geophys.* **2005**, *43*, RG2002. [CrossRef]

26. Silva Porfirio, A.C.; De Souza, J.L.; Bastos Lyra, G.; Maringolo Lemes, M.A. An assessment of the global UV solar radiation under various sky conditions in Maceió-Nottheastern Brazil. *Energy* **2012**, *44*, 584–592. [[CrossRef](#)]
27. Bilbao, J.; Mateos, D.; Yousif, C.; Román, R.; De Miguel, A. Influence of cloudiness on erythematous solar irradiance in Marsaxlokk, Malta: Two case studies. *Sol. Energy* **2016**, *136*, 475–486. [[CrossRef](#)]
28. Marín, M.J.; Serrano, D.; Utrillas, M.P.; Nunez, M.; Martínez-Lozano, J.A. Effective cloud optical depth and enhancement effects for broken liquid water clouds in Valencia (Spain). *Atmos. Res.* **2017**, *195*, 1–8. [[CrossRef](#)]
29. Turner, J.; Parisi, A.V. Ultraviolet reflection irradiances and exposures in the constructed environment for horizontal, vertical and inclined surfaces. *Photochem. Photobiol.* **2013**, *89*, 730–736. [[CrossRef](#)] [[PubMed](#)]
30. Seckmeyer, G.; Pissulla, D.; Glandorf, M.; Henriques, D.; Johnsen, B.; Webb, A. Variability of UV irradiance in Europe. *Photochem. Photobiol.* **2008**, *84*, 172–179. [[CrossRef](#)] [[PubMed](#)]
31. Silva, A.A.; Yamamoto, A.L.; Corrêa, M.P. Daily maximum erythematous dose rates in the tropics. *Photochem. Photobiol.* **2019**, *95*, 886–894. [[CrossRef](#)] [[PubMed](#)]
32. Burattini, C.; Pompei, L.; Salvadori, G.; Leccese, F.; Grignaffini, S.; Bisegna, F. Criticalities in monitoring the UV solar radiation for workers' safety. In Proceedings of the 21st IEEE International Conference on Environment and Electrical Engineering and 2021 5th IEEE Industrial and Commercial Power System Europe, IEEEIC/I and CPS Europe 2021, Bari, Italy, 7–10 September 2021; Code 176982. [[CrossRef](#)]
33. Allen, M.W.; Swift, N.; Nield, K.M.; Liley, B.; McKenzie, R.L. Use of Electronic UV Dosimeters in Measuring Personal UV Exposures and Public Health Education. *Atmosphere* **2020**, *11*, 744. [[CrossRef](#)]
34. Bisegna, F.; Burattini, C.; Pompei, L.; Rocca, M.; Leccese, F.; Salvadori, G.; Borra, M.; Militello, A. Broadband radiometers for the assessment of workers' exposure to UV radiation: Comparison of measurement results obtained with different devices. In Proceedings of the 2023 IEEE International Conference on Environment and Electrical Engineering and 2023 IEEE Industrial and Commercial Power Systems Europe (IEEEIC/I&CPS Europe), Madrid, Spain, 6–9 June 2023. [[CrossRef](#)]
35. Salvadori, G.; Leccese, F.; Lista, D.; Burattini, C.; Bisegna, F. Use of smartphone apps to monitor human exposure to solar radiation: Comparison between predicted and measured UV index values. *Environ. Res.* **2020**, *183*, 109274. [[CrossRef](#)]
36. Leccese, F.; Salvadori, G.; Lista, D.; Burattini, C. Outdoor Workers Exposed to UV Radiation: Comparison of UV Index Forecasting Methods. In Proceedings of the 2018 IEEE International Conference on Environment and Electrical Engineering and 2018 IEEE Industrial and Commercial Power Systems Europe, IEEEIC/I and CPS Europe 2018, Palermo, Italy, 12–15 June 2018. [[CrossRef](#)]
37. Militello, A.; Borra, M.; Bisegna, F.; Burattini, C.; Grandi, C. Smart Technologies: Useful Tools to Assess the Exposure to Solar Ultraviolet Radiation for General Population and Outdoor Workers. In Proceedings of the 18th Italian National Conference on Photonic Technologies, Rome, Italy, 6–8 June 2016. [[CrossRef](#)]
38. Gugliermetti, L.; Burattini, C.; Militello, A.; Borra, M.; Asdrubali, F.; Salvadori, G.; Leccese, F.; Bisegna, F. Real time UV erythematous personal exposure monitoring in outdoor workplaces. In Proceedings of the 2019 IEEE International Conference on Environment and Electrical Engineering and 2019 IEEE Industrial and Commercial Power Systems Europe (IEEEIC/I&CPS Europe), Genova, Italy, 11–14 June 2019. [[CrossRef](#)]
39. Salvadori, G.; Lista, D.; Burattini, C.; Gugliermetti, L.; Leccese, F.; Bisegna, F. Exposure of Body Districts: Development and Validation of an Algorithm to Predict the Erythematous Ultra Violet Dose. *Int. J. Environ. Res. Public Health* **2019**, *16*, 3632. [[CrossRef](#)]
40. Borra, M.; Grandi, C.; Militello, A.; Burattini, C.; Gugliermetti, L.; Mangione, A.; Bisegna, F.; Modenese, A.; Gobba, F. Developing an Algorithm to Assess the UV Erythematous Dose for Outdoor Workers. In Proceedings of the 2018 IEEE International Conference on Environment and Electrical Engineering and 2018 IEEE Industrial and Commercial Power Systems Europe, IEEEIC/I and CPS Europe 2018, Palermo, Italy, 12–15 June 2018. [[CrossRef](#)]
41. Gugliermetti, L.; Burattini, C.; Bisegna, F.; Militello, A.; Borra, M. Study on the positioning of a smart sensor for the assessment of UV radiation exposure in outdoor workers. In Proceedings of the 2019 IEEE International Conference on Environment and Electrical Engineering and 2019 IEEE Industrial and Commercial Power Systems Europe (IEEEIC/I&CPS Europe), Genova, Italy, 11–14 June 2019. [[CrossRef](#)]
42. Huang, X.; Chalmers, A.N. Review of Wearable and Portable Sensors for Monitoring Personal Solar UV Exposure. *Ann. Biomed. Eng.* **2021**, *49*, 964–978. [[CrossRef](#)]
43. Parisi, A.V.; Igoe, D.; Downs, N.J.; Turner, J.; Amar, A.; A Jebar, M.A. Satellite Monitoring of Environmental Solar Ultraviolet A (UVA) Exposure and Irradiance: A Review of OMI and GOME-2. *Remote Sens.* **2021**, *13*, 752. [[CrossRef](#)]
44. Singh, S.; Lodhi, N.K.; Mishra, A.K.; Jose, S.; Kumar, S.N.; Kotnala, R.K. Assessment of satellite-retrieved surface UVA and UVB radiation by comparison with ground-measurements and trends over Mega-city Delhi. *Atmos. Environ.* **2018**, *188*, 60–70. [[CrossRef](#)]
45. Utrillas, M.; Marín, M.; Esteve, A.; Salazar, G.; Suárez, H.; Gandía, S.; Martínez-Lozano, J. Relationship between erythematous UV and broadband solar irradiance at high altitude in Northwestern Argentina. *Energy* **2018**, *162*, 136–147. [[CrossRef](#)]
46. Malinović-Miličević, S.; Vyklyuk, Y.; Radovanović, M.M.; Petrović, M.D. Long-term erythematous ultraviolet radiation in Novi Sad (Serbia) reconstructed by neural network modelling. *Int. J. Clim.* **2018**, *38*, 3264–3272. [[CrossRef](#)]
47. VoPham, T.; Hart, J.E.; Bertrand, K.A.; Sun, Z.; Tamimi, R.M.; Laden, F. Spatiotemporal exposure modeling of ambient erythematous ultraviolet radiation. *Environ. Health* **2016**, *15*, 111. [[CrossRef](#)] [[PubMed](#)]

48. Buntoung, S.; Janjai, S.; Nunez, M.; Choosri, P.; Pratummasoot, N.; Chiwpreecha, K. Sensitivity of erythemal UV/global irradiance ratios to atmospheric parameters: Application for estimating erythemal radiation at four sites in Thailand. *Atmos. Res.* **2014**, *149*, 24–34. [[CrossRef](#)]
49. Kosmopoulos, P.G.; Kazadzis, S.; Schmalwieser, A.W.; Raptis, P.I.; Papachristopoulou, K.; Fountoulakis, I.; Masoom, A.; Bais, A.F.; Bilbao, J.; Blumthaler, M.; et al. Real-time UV index retrieval in Europe using Earth observation-based techniques: System description and quality assessment. *Atmos. Meas. Tech.* **2021**, *14*, 5657–5699. [[CrossRef](#)]
50. Lakkala, K.; Kujanpää, J.; Brogniez, C.; Henriot, N.; Arola, A.; Aun, M.; Auriol, F.; Bais, A.F.; Bernhard, G.; De Bock, V.; et al. Validation of the TROPOspheric Monitoring Instrument (TROPOMI) surface UV radiation product. *Atmos. Meas. Tech.* **2020**, *13*, 6999–7024. [[CrossRef](#)]
51. Emde, C.; Buras-Schnell, R.; Kylling, A.; Mayer, B.; Gasteiger, J.; Hamann, U.; Kylling, J.; Richter, B.; Pause, C.; Dowling, T.; et al. The libRadtran software pack-age for radiative transfer calculations (version 2.0.1). *Geosci. Model. Dev.* **2016**, *9*, 1647–1672. [[CrossRef](#)]
52. Madronich, S.; Flocke, S. *Theoretical Estimation of Biologically Effective UV Radiation at the Earth's Surface*, in *Solar Ultraviolet Radiation—Modeling, Measurements and Effects*; Zerefos, C., Ed.; NATO ASI Series; Springer: Berlin, Germany, 1997; Volume 52. [[CrossRef](#)]
53. Ricchiazzi, P.; Yang, S.; Gautier, C.; Sowle, D. SBDART: A research and teaching software tool for plane-parallel radiative transfer in the Earth's atmosphere. *Bull. Am. Meteorol. Soc.* **1998**, *79*, 2101–2114. [[CrossRef](#)]
54. De Paula Correa, M. UVBoost: An erythemal weighted ultraviolet radiation estimator based on machine learning gradient boosting algorithm. *J. Quant. Spectrosc. Radiat. Transf.* **2023**, *298*, 108490. [[CrossRef](#)]
55. Kazantzidis, A.; Smedley, A.; Kift, R.; Rimmer, J.; Berry, J.L.; Rhodes, L.E.; Webb, A.R. A modeling approach to determine how much UV radiation is available across the UK and Ireland for health risk and benefit studies. *Photochem. Photobiol. Sci.* **2015**, *14*, 1073. [[CrossRef](#)]
56. Malinovic-Milicevic, S.; Mihailovic, D.T.; Radovanovic, M.M. Reconstruction of the erythemal UV radiation data in Novi Sad (Serbia) using the NEOPLANTA parametric model. *Theor. Appl. Climatol.* **2015**, *121*, 131–138. [[CrossRef](#)]
57. García-Rodríguez, S.; García-Rodríguez, A.; Granados-López, D.; García, I.; Alonso-Tristán, C. Ultraviolet Erythemal Irradiance (UVER) under Different Sky Conditions in Burgos, Spain: Multilinear Regression and Artificial Neural Network Models. *Appl. Sci.* **2023**, *13*, 10979. [[CrossRef](#)]
58. González-Rodríguez, L.; de Oliveira, A.P.; Rodríguez-López, L.; Rosas, J.; Contreras, D.; Baeza, A.C. A Study of UVER in Santiago, Chile Based on Long-Term In Situ Measurements (Five Years) and Empirical Modelling. *Energies* **2021**, *14*, 368. [[CrossRef](#)]
59. Boers, R.; Mitchell, R.M.; Krummel, P.B. Correction of aircraft pyranometer measurements for diffuse radiance and alignment errors. *J. Geophys. Res.* **1998**, *103*, 16753–16758. [[CrossRef](#)]
60. Webb, A.R.; Weihs, P.; Blumthaler, M. Spectral UVR irradiance on vertical surfaces: A case study. *Photochem. Photobiol.* **1999**, *69*, 464–470. [[CrossRef](#)]
61. Parisi, A.V.; Kimlin, M.G. Horizontal and sun-normal spectral biologically effective ultraviolet irradiances. *Photochem. Photobiol.* **1999**, *53*, 70–74. [[CrossRef](#)]
62. Oppenrieder, A.; Hoeppe, P.; Koepke, P. Routine measurement of erythemally effective UV irradiances on inclined surfaces. *Photochem. Photobiol.* **2004**, *74*, 85–94. [[CrossRef](#)]
63. Hu, L.W.; Gong, H.Z.; Jun Yu, D.; Gao, Q.; Gao, N.; Wang, M.; Yan, Y.; Wang, Y.; Yu, J.; Liu, Y. Diurnal Variations in Solar Ultraviolet Radiation on Horizontal and Vertical Plane. *Iran. J. Public Health* **2010**, *39*, 70–81.
64. Soueid, L.; Triguero-Mas, M.; Dalmau, A.; Berrera-Gòmez, J.; Alonso, L.; Basagaña, X.; Thieden, E.; Wulf, H.C.; Diffey, B.; Young, A.R.; et al. Estimating personal solar ultraviolet radiation exposure through time spent outdoors, ambient levels and modelling approaches. *Br. J. Dermatol.* **2022**, *186*, 266–273. [[CrossRef](#)]
65. Vernez, D.; Milon, A.; Vuillemier, L.; Buillard, J.-L.; Koechlin, A.; Boniol, M.; Doré, J.F. A general model to predict individual exposure to solar UV by using ambient irradiance data. *J. Expo. Sci. Environ. Epidemiol.* **2015**, *25*, 113–118. [[CrossRef](#)]
66. Schmalwieser, A.W.; Lohr, M.A.; Daly, S.M.; Williams, J.D. Modelling acute and cumulative erythemal sun exposure on vulnerable body sites during beach vacation utilizing behavior-encoded 3D body models. *Photochem. Photobiol.* **2023**, *22*, 1–20.
67. Cheng, W.; Brown, R.; Vernez, D.; Goldberg, D. Estimation of Individual Exposure to Erythemal Weighted UVR by Multi-Sensor Measurements and Integral Calculation. *Sensors* **2020**, *20*, 4068. [[CrossRef](#)]

Disclaimer/Publisher's Note: The statements, opinions and data contained in all publications are solely those of the individual author(s) and contributor(s) and not of MDPI and/or the editor(s). MDPI and/or the editor(s) disclaim responsibility for any injury to people or property resulting from any ideas, methods, instructions or products referred to in the content.